

Multivariate Fields of Experts

Stanislas Ducotterd and Michael Unser

Abstract—We introduce the multivariate fields of experts, a new framework for the learning of image priors. Our model generalizes existing fields of experts methods by incorporating multivariate potential functions constructed via Moreau envelopes of the ℓ_∞ -norm. We demonstrate the effectiveness of our proposal across a range of inverse problems that include image denoising, deblurring, compressed-sensing magnetic-resonance imaging, and computed tomography. The proposed approach outperforms comparable univariate models and achieves performance close to that of deep-learning-based regularizers while being significantly faster, requiring fewer parameters, and being trained on substantially fewer data. In addition, our model retains a relatively high level of interpretability due to its structured design.

Index Terms—Learnable regularizer, variational methods, inverse problems, Moreau envelope.

I. INTRODUCTION

In many areas of science and engineering, it is common to recover an object of interest from indirect linear measurements. Let $\mathbf{H} \in \mathbb{R}^{m \times n}$ denote the measurement operator and let $\mathbf{y} \in \mathbb{R}^m$ be the observed data. The goal is to reconstruct the underlying signal $\mathbf{x} \in \mathbb{R}^n$ such that $\mathbf{H}\mathbf{x} \approx \mathbf{y}$. However, since \mathbf{y} is usually noisy and \mathbf{H} is often ill-conditioned or even rank-deficient, the direct inversion is typically unstable and results in poor reconstructions. To address this, a popular strategy is to use variational regularization to recover \mathbf{x} as the minimizer of the energy

$$\frac{1}{2} \|\mathbf{H}\mathbf{x} - \mathbf{y}\|_2^2 + \lambda R(\mathbf{x}), \quad (1)$$

where the first term enforces data fidelity and where the regularizer $R: \mathbb{R}^n \rightarrow \mathbb{R}$ encodes prior knowledge about the underlying data.

Many popular regularizers [1]–[7] can be expressed as a sum of pointwise potential functions applied to the data convolved with a filter. In particular, the weakly convex ridge regularizer (WCRR) [5] represents a recent advance in this direction, where univariate nonconvex potentials are learned via linear splines.

In this work, we propose the multivariate fields of experts¹ (MFoE), a novel class of learned regularizers that extends the classic fields of experts (FoE) framework by incorporating multivariate potential functions. Our contributions are as follows.

- We introduce a class of parametric potentials that almost exactly reproduce the spline-based potentials learned in WCRR;

- we extend WCRR to the multivariate setting by incorporating the ℓ_∞ -norm into this parametric potential framework;
- we demonstrate the effectiveness of our approach across multiple inverse problems: denoising, deblurring, compressed-sensing magnetic-resonance imaging (CS-MRI), and computed tomography (CT).

II. RELATED WORK

A popular model for image reconstruction is the total variation (TV) regularizer [8], where the regularization term R promotes piecewise-constant solutions by penalizing the horizontal and vertical finite differences of the image. Since R is not differentiable, the objective (1) is typically minimized via the proximal operator

$$\text{prox}_{\lambda R}(\mathbf{y}) = \arg \min_{\mathbf{x} \in \mathbb{R}^n} \left(\frac{1}{2} \|\mathbf{x} - \mathbf{y}\|_2^2 + \lambda R(\mathbf{x}) \right), \quad (2)$$

which yields the solution of a denoising problem—the simplest instance of (1) with $\mathbf{H} = \mathbf{I}$. This proximal operator does not admit a closed-form solution and must be computed using iterative algorithms [9].

To further improve the reconstruction performance of variational methods, many works have proposed data-driven approaches to construct R . The FoE framework [1] introduced a regularizer defined, for any image $\mathbf{x} \in \mathbb{R}^n$, as

$$R(\mathbf{x}) = \sum_{k=1}^K \langle \mathbf{1}_n, \psi_k(\mathbf{W}_k \mathbf{x}) \rangle, \quad (3)$$

where $\mathbf{W}_k \in \mathbb{R}^{n \times n}$ denotes a convolution matrix and $\psi_k: \mathbb{R} \rightarrow \mathbb{R}$ is a pointwise nonlinearity. In the original FoE model, the potentials ψ_k correspond to the negative log-likelihood of Student- t distributions and the filters $\{\mathbf{W}_k\}_{k=1}^K$ are learned by the minimization of $\sum_{m=1}^M R(\mathbf{x}_m)$ over a dataset $\{\mathbf{x}_m\}_{m=1}^M$ of natural images.

A more advanced strategy for the learning of the regularizer was proposed in [2], where bilevel optimization [10] is employed. In this setting, the filters are trained to minimize the denoising loss

$$\sum_{m=1}^M \|\text{prox}_{\lambda R}(\mathbf{x}_m + \mathbf{n}_m) - \mathbf{x}_m\|_2^2, \quad (4)$$

where \mathbf{n}_m is additive white Gaussian noise. Although the potentials $\{\psi_k\}_{k=1}^K$ are generally nonconvex in FoE, which makes the proximal operator $\text{prox}_{\lambda R}$ potentially set-valued, bilevel optimization remains applicable and effective in practice.

Subsequent works [3]–[7] have further increased expressivity of the FoE model by jointly learning the filters and the nonlinearities $\{\psi_k\}_{k=1}^K$. While the WCRR learns the

^{*}The authors are with the Biomedical Imaging Group, École Polytechnique Fédérale de Lausanne (EPFL), {forename.name}@epfl.ch.

¹<https://github.com/StanislasDucotterd/MFoE>

gradient of R by parameterizing the derivatives of univariate potentials with linear splines, our model extends the approach to the multivariate setting using higher-dimensional potential functions.

Another important framework for image reconstruction is plug-and-play (PnP) [11], where an off-the-shelf denoiser is inserted as a surrogate for the proximal operator in iterative optimization algorithms. While PnP methods are inspired by variational formulations, they generally do not correspond to the minimization of a well-defined energy functional and therefore lack convergence guarantees in general. Several strategies have been proposed to address this issue, such as Lipschitz constraints on the denoiser [12], [13], or continuation schemes [14] that gradually reduce the influence of the denoiser over the course of optimization.

Finally, a recent line of work have bridged the gap between variational methods and the PnP framework by learning an explicit regularizer $R: \mathbb{R}^n \rightarrow \mathbb{R}$ using deep neural networks [15]–[17]. These methods supervise the model via its gradient ∇R , which requires the computation of second-order derivatives during training. This yields highly expressive regularizers with an explicit objective and general convergence guarantees, but comes at the cost of significant computational overhead—both during training, due to the need to differentiate the objective twice, and at inference time, where the gradient of the neural network must be evaluated at each optimization step.

III. DESCRIPTION OF THE MODEL

A. Notations and Definitions

The least-squares projection onto a set \mathcal{C} is defined as

$$\text{Proj}_{\mathcal{C}}(\mathbf{x}) = \arg \min_{\mathbf{z} \in \mathcal{C}} \|\mathbf{z} - \mathbf{x}\|_2^2. \quad (5)$$

This projection exists and is unique whenever the set \mathcal{C} is closed and convex. A particular closed convex set of interest in this work is the ℓ_1 -ball in \mathbb{R}^d , which we denote by

$$\mathcal{B}_{\ell_1} = \{\mathbf{z} \in \mathbb{R}^d : \|\mathbf{z}\|_1 \leq 1\}. \quad (6)$$

The Moreau envelope [18] of a proper, lower semi-continuous, convex function $f: \mathbb{R}^d \rightarrow \mathbb{R}$ with parameter $\mu > 0$ is defined as

$$M_f^\mu(\mathbf{x}) = \inf_{\mathbf{z} \in \mathbb{R}^d} \left(f(\mathbf{z}) + \frac{1}{2\mu} \|\mathbf{z} - \mathbf{x}\|_2^2 \right). \quad (7)$$

The gradient of the Moreau envelope of f can be related to the proximal operator of f through the equality

$$\nabla M_f^\mu(\mathbf{x}) = \frac{1}{\mu} (\mathbf{x} - \text{prox}_{\mu f}(\mathbf{x})). \quad (8)$$

In this paper, we denote the Moreau envelope (with parameter μ) of the ℓ_∞ -norm in \mathbb{R}^d as $\rho_d^\mu: \mathbb{R}^d \rightarrow \mathbb{R}_+$. Using the definition in (7) and the identity

$$\text{prox}_{\mu \|\cdot\|_\infty}(\mathbf{x}) = \mathbf{x} - \mu \text{Proj}_{\mathcal{B}_{\ell_1}}(\mathbf{x}/\mu) \quad (9)$$

with $\mathbf{x} \in \mathbb{R}^d$, we can write that

$$\rho_\mu^d(\mathbf{x}) = \|\mathbf{x} - \mu \text{Proj}_{\mathcal{B}_{\ell_1}}(\mathbf{x}/\mu)\|_\infty + \frac{\mu}{2} \|\text{Proj}_{\mathcal{B}_{\ell_1}}(\mathbf{x}/\mu)\|_2^2. \quad (10)$$

From (8), we then obtain the gradient

$$\nabla \rho_\mu^d(\mathbf{x}) = \text{Proj}_{\mathcal{B}_{\ell_1}}(\mathbf{x}/\mu), \quad (11)$$

which is computed via sorting using the Condat algorithm [19].

B. Generalization of the WCRR

In Figure 1, we illustrate that the potential learned via linear splines with more than 100 knots in the WCRR can be approximated almost to perfection by a simple parametric form with three degrees of freedom: Indeed, the function $t \mapsto \lambda(\rho_1^\mu(t) - \rho_1^\nu(t))$ with $\mu = 0.002$ and $\lambda = \nu = 0.098$ is visually indistinguishable from the WCRR of Figure 1. This type of potential is close to the minimax-concave penalty introduced in [20]. This observation motivates the use of ρ_d^μ as a foundation for a multivariate extension, with the property that the model can reduce to the WCRR when $d = 1$.

Note that the absolute value is the only one-dimensional function (up to scaling) that is a norm. This suggests to extend it by the consideration of the Moreau envelopes of general norms. We focus on norms for which both the Moreau envelope and its gradient can be computed efficiently. Among the classic choices, the ℓ_2 and ℓ_∞ norms are particularly tractable. We opt for the ℓ_∞ norm for two main reasons: first, it empirically leads to better reconstruction results; second, as established in [21], any norm can be approximated arbitrarily well by the composition of the ℓ_∞ norm with a linear transformation. This makes it a particularly expressive and computationally attractive choice for multivariate potentials.

The WCRR constrains its potentials to be 1-weakly convex to ensure overall convexity during denoising, given the 1-strong convexity of the data term. While this has minimal impact in the univariate case, it limits performance in the multivariate setting. We therefore relax this constraint in our model and allow potentials with larger weak-convexity constants. To isolate the effect of our multivariate formulation from that of the relaxation, we also compare against a relaxed version of WCRR.

C. General Setting

We now move beyond the one-dimensional setting and extend the FoE framework to the multivariate case, where the regularizer is defined, for any image $\mathbf{x} \in \mathbb{R}^n$, as

$$R(\mathbf{x}) = \sum_{k=1}^K \langle \mathbf{1}_n, \psi_k^d(\mathbf{W}_k^d \mathbf{x}) \rangle, \quad (12)$$

where $\mathbf{W}_k^d \in \mathbb{R}^{(dn) \times n}$ denotes a convolution matrix that maps a single-channel image to a d -channel one, and $\psi_k^d: \mathbb{R}^d \rightarrow \mathbb{R}$ is a nonlinearity given by

$$\psi_k(\mathbf{x}) = \mu_k \rho_{\mu_k}^d(\mathbf{x}) - \mu_k \rho_{\tau_k \mu_k}^d(\mathbf{Q}_k \mathbf{x}), \quad (13)$$

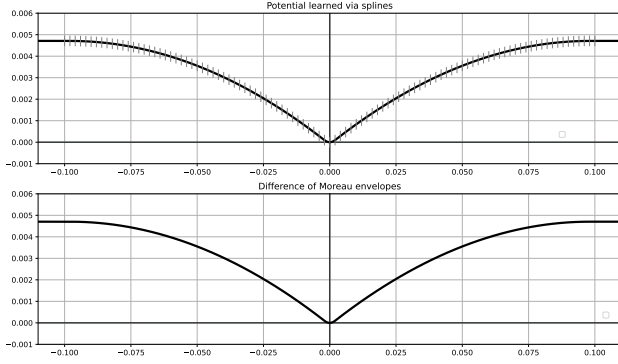


Fig. 1. Top: Potential learned in WCRR, vertical lines mark the spline control points. Bottom: Difference between two Moreau envelopes of the absolute value with different parameters.

where $\mathbf{Q}_k \in \mathbb{R}^{d \times d}$ and τ_k is a scalar.

Theorem 1: If \mathbf{Q}_k is such that $\|\mathbf{Q}_k\|_\infty \leq 1$ and $\tau_k > \|\mathbf{Q}_k\|_2^2$, then the nonlinearity defined in (13) is nonnegative with a unique global minimum at the origin and has nonexpansive gradients.

Theorem 1 guarantees that the regularizer is bounded from below and preserves a similar interpretation to the classic FoE, where weak filter responses are favored while stronger responses are increasingly penalized. The proof can be found in Appendix A.

The gradient of our regularizer can be written as

$$\nabla R(\mathbf{x}) = \mathbf{W}^T \varphi(\mathbf{W}\mathbf{x}), \quad (14)$$

where $\mathbf{W} \in \mathbb{R}^{(Kdn) \times n}$ refers to the concatenation of all the d -channel convolutions \mathbf{W}_k^d and φ refers to the concatenation of all the gradients $\nabla \psi_k: \mathbb{R}^d \rightarrow \mathbb{R}^d$. The spectral norm of the filters $\|\mathbf{W}\|_2$ is enforced to be one via the same methods as in [5], which ensures that ∇R is nonexpansive.

We train the filters \mathbf{W} , the K matrices \mathbf{Q}_k , scalars μ_k, τ_k , and the regularizing strength λ to minimize the denoising loss (4).

To efficiently train filters with a large receptive field, we decompose \mathbf{W} into a composition of three zero-padded convolutions with small kernels and an increasing number of output channels as in [4]. Similarly to [22], the filters are constrained to have zero mean.

D. Optimization

We minimize the objective (1) using accelerated gradient descent with restart based on the value of the objective as described in [23]. We give the pseudocode for our implementation in Algorithm 1 where f corresponds to (1). Throughout the paper, we set

$$\gamma = \frac{1}{\|\mathbf{H}\|_2^2 + \lambda}. \quad (15)$$

Since the regularizer has a gradient ∇R that is nonexpansive, the Lipschitz constant of the gradient of (1) is upper-bounded

Algorithm 1 Accelerated gradient descent with restart based on the objective

Input: Function f , stepsize γ , initialization $\mathbf{x}_0 \in \mathbb{R}^d$, tolerance $\varepsilon > 0$, number of iterations n_{\max}

- 1: Set $t_0 = 1, k = 0, r_0 = \infty, f_0 = \infty, \mathbf{z}_0 = \mathbf{x}_0$
- 2: **while** $r_k > \varepsilon$ and $k \leq n_{\max}$ **do**
- 3: $\mathbf{x}_{k+1} = \mathbf{z}_k - \gamma \nabla f(\mathbf{z}_k)$
- 4: $f_{k+1} = f(\mathbf{z}_k)$
- 5: $t_{k+1} = \frac{1 + \sqrt{1 + 4t_k^2}}{2}$
- 6: $\mathbf{z}_{k+1} = \mathbf{x}_{k+1} + \frac{t_k - 1}{t_{k+1}}(\mathbf{x}_{k+1} - \mathbf{x}_k)$
- 7: **if** $f_{k+1} > f_k$ **then**
- 8: $\mathbf{z}_{k+1} = \mathbf{x}_{k+1}$
- 9: $t_{k+1} = 1$
- 10: **end if**
- 11: $r_{k+1} = \|\mathbf{x}_{k+1} - \mathbf{x}_k\| / \|\mathbf{x}_{k+1}\|$
- 12: $k \leftarrow k + 1$
- 13: **end while**

Output: Approximate solution \mathbf{x}_{k+1}

by the Lipschitz constant of the data-fitting term plus the regularization parameter λ .

The computational cost of the fourth line of Algorithm 1 turns out to be negligible, due to the nature of our potentials. Indeed, from (10) and (11), we have that

$$\rho_d^\mu(\mathbf{x}) = \|\mathbf{x} - \mu \nabla \rho_d^\mu(\mathbf{x})\|_\infty + \frac{\mu}{2} \|\nabla \rho_d^\mu(\mathbf{x})\|_2^2, \quad (16)$$

which makes it very easy to compute the objective on top of the gradient. Therefore, the restart strategy allows us to decrease the amount of iterations without increasing the time required to do one.

E. Dependence on the Noise Level

To make our regularizer more universal, we train it on a range of Gaussian-noise levels and denote by R_σ the regularizer associated with the noise level σ . To keep the model as simple as possible, we share the filters and most other parameters across noise levels, allowing only $\{\mu_k\}_{k=1}^K$ to depend on σ . We define a function $\boldsymbol{\mu}: \mathbb{R} \rightarrow \mathbb{R}^K$ that concatenates the μ_k , such that $\mu_k(\sigma) = \mu(\sigma)_k$. This function is parameterized as

$$\boldsymbol{\mu}(\sigma) = \frac{1}{100} \left(\sigma \cdot \mathbf{1}_K + \frac{1}{20} \mathbf{f}(\bar{\sigma}) \right)_+ + 10^{-9} \cdot \mathbf{1}_K, \quad (17)$$

where $\mathbf{f}: \mathbb{R} \rightarrow \mathbb{R}^K$ is a three-layer neural network. The function $(\cdot)_+ := \max(0, \cdot)$ and the addition of a small term are here to ensure that components of $\boldsymbol{\mu}$ stay positive. The term $\bar{\sigma}$ refers to a min-max normalization of σ such that it is in the interval $[-2, 2]$ in order to fully benefit from the neural network \mathbf{f} whose knots at initialization are mostly located in that range.

IV. EXPERIMENTS

A. Training on Denoising

We denote by $\boldsymbol{\theta}$ the vector of all parameters in our model. The paired data used for training are $(\mathbf{x}_m, \mathbf{y}_m)_{m=1}^M$, where

each noisy observation is generated as $\mathbf{y}_m = \mathbf{x}_m + \sigma_m \mathbf{n}_m$ with Gaussian noise $\mathbf{n}_m \sim \mathcal{N}(\mathbf{0}, \mathbf{I})$ and noise levels $\sigma_m \sim \mathcal{U}(0, 0.2)$. The model is trained to minimize the reconstruction loss

$$\mathcal{L}(\boldsymbol{\theta}) = \frac{1}{M} \sum_{m=1}^M \frac{1}{\sqrt{\sigma_m}} \|\mathbf{x}_m^* - \mathbf{x}_m\|_1, \quad (18)$$

where $\mathbf{x}_m^* \in \text{prox}_{\lambda R_{\sigma_m}}(\mathbf{y}_m)$. The weighting by $1/\sqrt{\sigma_m}$ ensures that the model gives sufficient importance to low noise levels during training.

We follow a bilevel strategy to optimize (18). The inner optimization corresponds to the solution \mathbf{x}_m^* to the proximal problem in (2), as found through accelerated gradient descent with restarts, as described in Algorithm 1. The inner loop terminates when the relative change of the iterates falls below 10^{-4} or after 300 iterations.

The outer optimization aims to learn $\boldsymbol{\theta}$ by minimizing the empirical loss (18). This is done using gradient-based optimization with implicit differentiation to compute the required gradients within the inner-optimization process. We use the `torchdeq` library [24] and apply 25 steps of the Broyden algorithm [25] to approximate the gradient of the fixed-point solution.

The training is conducted on a dataset of 238,400 small patches of size (40×40) , extracted from 400 images from the BSD500 dataset [26] and scaled to $[0, 1]$. This number of training images is relatively small compared to typical deep-learning-based methods, which often rely on significantly bigger datasets to achieve good generalization [27]. We use the ADAM optimizer with a batch size of 128, setting the learning rate to 0.005 for the filters \mathbf{W} and the function $\boldsymbol{\mu}$, while all other parameters use a learning rate of 0.05. The model is trained for 5000 steps, and the learning rates are decayed by a factor of 0.75 every 500 steps. The full training procedure takes around 5.5 hours on a Tesla V100 GPU.

We report the denoising performance of MFoE in Table I, using $K = 15$ potentials of input dimension $d = 4$ with filters of size (11×11) . For comparison purposes, we include TV [8], the WCRR [5] and Prox-DRUNet [16]. Note that the WCRR results differ slightly from those in the original paper, as we trained it on noise levels ranging from 0 to 50/255, whereas the original implementation was ranging from 0 to 30/255. We achieved this by modifying only the splines s_{α_i} from [5, Equation (17)], increasing the number of knots from 11 to 18 to maintain interval lengths as close as possible to the original configuration.

As mentioned in Section III-B, we add the relaxed version of WCRR (WCRR-free) and an alternative version of our model based on the ℓ_2 -norm (MFoE- ℓ_2). More details about their implementation can be found in Appendices B and C.

Relaxing the 1-weak convexity constraint in WCRR does not yield performance improvements, except at the highest noise level. In contrast, the proposed MFoE model consistently outperforms the univariate baselines (WCRR and WCRR-free) as well as the multivariate variant MFoE- ℓ_2 . Notably, all four models employ the same number of filters ($Kd = 60$) and have roughly the same number of parameters, which

TABLE I
DENOISING PERFORMANCE IN TERMS OF NOISE LEVEL ON THE BSD68 TEST SET.

	$\sigma = 15/255$	$\sigma = 25/255$	$\sigma = 50/255$	Parameters
TV	29.90	27.48	24.83	1
WCRR	31.20	28.68	25.68	$1.4 \cdot 10^4$
WCRR-free	31.18	28.68	25.78	$1.4 \cdot 10^4$
MFoE- ℓ_2	31.22	28.71	25.80	$1.4 \cdot 10^4$
MFoE	31.32	28.84	25.92	$1.4 \cdot 10^4$
Prox-DRUNet	31.70	29.18	26.13	$1.7 \cdot 10^7$

TABLE II
DENOISING PERFORMANCE IN TERMS OF NOISE LEVEL ON THE BSD68 TEST SET.

	$\sigma = 15/255$	$\sigma = 25/255$	$\sigma = 50/255$
MFoE ($K = 15, d = 4$)	31.32	28.84	25.92
MFoE ($K = 30, d = 4$)	31.36	28.88	25.97
MFoE ($K = 45, d = 4$)	31.38	28.90	25.99
MFoE ($K = 60, d = 4$)	31.39	28.90	25.97

ensures that the observed performance gains are not due to increased model capacity but result instead from the greater expressiveness of the proposed multivariate potentials.

We present in Table II the performance of the MFoE as we increase the number of filters from $Kd = 60$ to 240. Unlike the WCRR, which saturates at 60 filters, our model continues to improve and reaches a performance plateau around 180 filters. To ensure fair comparisons throughout the paper, we adopt the 60-filter variant as our default model.

We further investigate the tradeoff between K and d in Table VII, keeping the total number of filters fixed at $Kd = 60$. We observe a significant improvement when moving from $d = 1$ to $d = 2$, with performance peaking at $d = 4$. Beyond that, performance degrades steadily, with $d = 60$ performing worse than even the univariate case $d = 1$.

B. Visualization and Analysis of the Learned Model

We display the filters of the ($K = 15, d = 4$) model in Figure 2. Filters within the same group tend to exhibit similar and complementary structures, while filters across different groups often vary significantly. Since the potential function depends primarily on the filter that produces the strongest response, this behavior suggests a form of invariance in the model—possibly to orientation, scale, or other transformations.

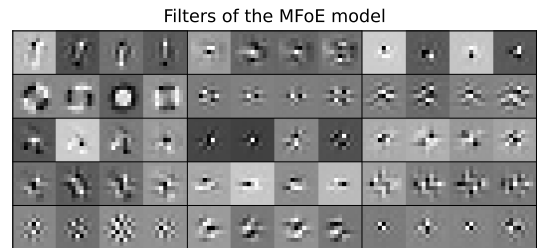


Fig. 2. Learned filters on the denoising task with $K = 15$ and $d = 4$. The black lines split the filters into the 15 different groups of 4.

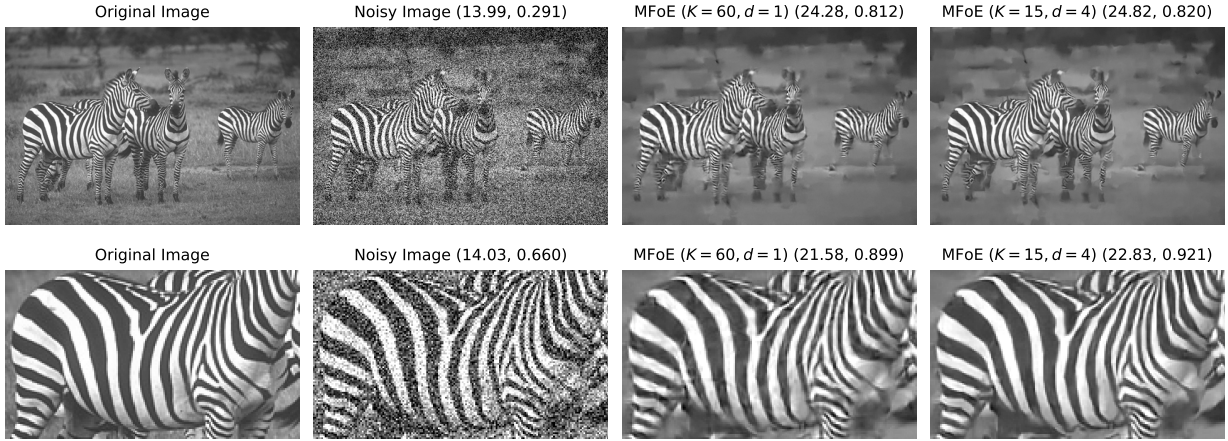


Fig. 3. Denoising results for $\sigma = 0.2$, shown on the full image and on a zoomed-in textured region. The reported metrics are (PSNR, SSIM).

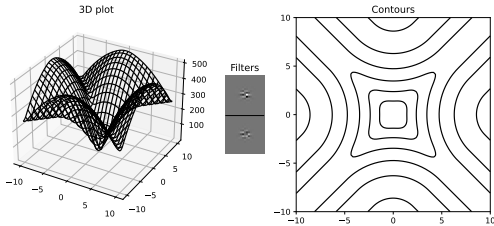


Fig. 4. Learned potential function and the corresponding filters.

We also plot a learned potential of the $(K = 30, d = 2)$ model along with its two corresponding filter in Figure 4 and show two additional ones in Section E.

A direct corollary of Theorem 1 is that the minimizers of our regularizer lie in the null space of \mathbf{W} . In Figure 5, we show the impulse response of the filter that corresponds to $\mathbf{W}^T \mathbf{W}$, along with the magnitude of its Fourier transform. While the impulse response is close to a Kronecker impulse, it cannot be exactly so as it must sum up to zero due to the zero-mean constraint on all filters in \mathbf{W} . The frequency response reveals that only the zero-frequency coefficient vanishes, which suggests that the null space of \mathbf{W} is one-dimensional and consists of constant images. However, this is not entirely accurate: because our filters are zero-padded, $\mathbf{W}^T \mathbf{W}$ is not perfectly diagonalized by the discrete Fourier transform—although the approximation is very close, as shown in [28]. It is also intuitive that nonzero constant images are not in the null space of \mathbf{W} , as the discontinuities they create at the boundaries result in nonzero filter responses.

To complete the analysis, we run power iterations on $(\mathbf{I} - \mathbf{W}^T \mathbf{W})$ in `float64` precision to accurately estimate the smallest singular value of \mathbf{W} . The result, in excess of $2.5 \cdot 10^{-3}$, shows that the null space of \mathbf{W} is empty. Consequently, our regularizer admits a unique global minimum, the zero-valued image.

A qualitative comparison of denoising results between our model and univariate baselines reveals that our approach performs particularly well in high-frequency regions that resemble textures as shown in Figure 3. This observation aligns with

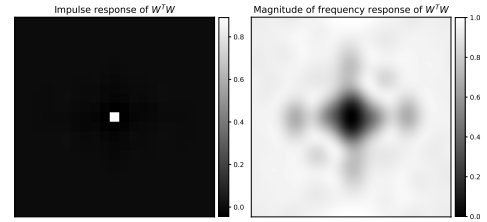


Fig. 5. Impulse and frequency response of $\mathbf{W}^T \mathbf{W}$. The image size on the left is (21×21) , identical to the size of $\mathbf{W}^T \mathbf{W}$. The image size on the right is (1500×1500) , which accommodates for some amount of zero-padding in the Fourier transform.

techniques used in classic texture-classification frameworks [29], [30], where features are derived from the strongest response across a bank of filters with varying orientations and scales.

C. Inverse Problems

We benchmark MFoE for image deblurring, CS-MRI, and CT. For this, we simulate measurements as

$$\mathbf{y} = \mathbf{H}\mathbf{x} + \mathbf{w}, \quad (19)$$

where \mathbf{H} is the linear operator that corresponds to the imaging modality and $\mathbf{w} \sim \mathcal{N}(\mathbf{0}, \sigma_{\mathbf{w}} \mathbf{I})$.

We compare our learned regularizer with TV, the WCRR, and Prox-DRUNet. Image reconstruction with these methods requires the minimization of the objective (1). This is done via an iterative optimization algorithm which is terminated when the relative difference of the iterates is below 10^{-5} or when the number of iterations exceeds 1000.

To deploy the models, we tune their hyperparameters on a validation set using the coarse-to-fine grid search from [4]. Then, the performance is reported on a dedicated test set. For TV, we only tune the regularization strength λ in (1). For the other methods, we tune λ and the noise level σ .

1) *Deblurring*: We evaluate the frameworks on a deblurring task, where \mathbf{H} is a convolution operator. We took from [31] three kernels of size (25×25) shown on the top of

TABLE III
PSNR VALUES FOR THE DEBLURRING ON THE BSD68 DATASET.

						
	$\sigma_w = 0.01$	$\sigma_w = 0.03$	$\sigma_w = 0.01$	$\sigma_w = 0.03$	$\sigma_w = 0.01$	$\sigma_w = 0.03$
TV	26.74	25.62	29.16	26.17	29.36	26.05
WCRR	27.25	26.09	30.26	26.88	30.38	26.75
MFoE	27.36	26.18	<u>30.43</u>	<u>27.14</u>	<u>30.65</u>	<u>27.04</u>
Prox-DRUNet	<u>27.34</u>	<u>26.17</u>	30.55	27.24	30.78	27.15

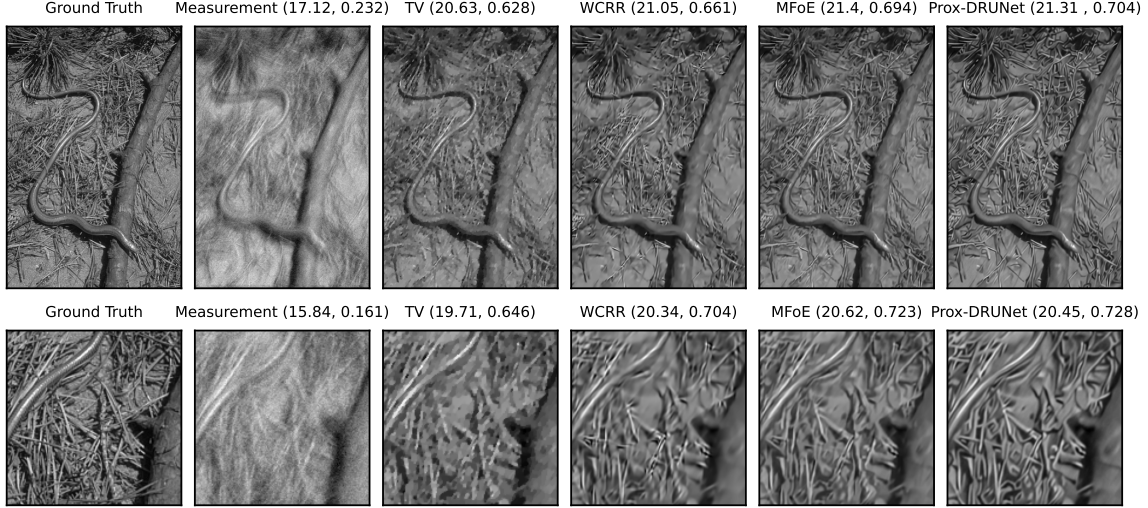


Fig. 6. Reconstruction for a blur with the third kernel and $\sigma_w = 0.03$. The reported metrics are (PSNR, SSIM).

Table III. One kernel is isotropic Gaussian and the other two are anisotropic kernels that correspond to a motion blur. We evaluate the noise levels $\sigma_w \in \{0.01, 0.03\}$. Each method is initialized with the observed blurred and noisy measurements, the hyperparameters are tuned on the Set12 dataset, and the performances are reported on the BSD68 dataset.

We report the performances in Table III. The MFoE outperforms the WCRR in every instance and manages to match the performances of Prox-DRUNet for the isotropic blur. Examples of deblurring are provided in Figure 6. There, we can see in the zoomed part that Prox-DRUNet makes a somewhat bolder prediction than the other models. This results in a higher SSIM but a slightly lower PSNR than MFoE, despite its blurrier prediction.

2) *Compressed-Sensing MRI*: We use fully sampled knee images of size (320×320) from the fastMRI dataset [32] as ground truth, including scans with (PDFS) and without (PD) fat suppression. The corresponding measurements are obtained by a subsampling of the 2D Fourier transform (k -space) using a Cartesian sampling mask defined by two parameters: the acceleration factor M_{acc} and the center fraction M_{cf} . Specifically, the central $\lfloor 320M_{cf} \rfloor$ columns of k -space (those corresponding to low frequencies) are fully retained, while the remaining columns are uniformly subsampled, which results in a total of $\lfloor 320/M_{acc} \rfloor$ selected columns. Gaussian noise with standard deviation $\sigma_w = 0.01$ is added to the real and the imaginary part of the measurements. Each method is initialized with the zero-filled image, the hyperparameters are

TABLE IV
PSNR VALUES FOR MRI RECONSTRUCTION ON THE FASTMRI DATASET.

	$(M_{acc} = 4, M_{cf} = 0.08)$		$(M_{acc} = 8, M_{cf} = 0.04)$	
	PD	PDFS	PD	PDFS
Zero-fill	27.43	29.62	23.49	27.00
TV	33.23	32.70	26.97	29.42
WCRR	35.10	34.18	29.32	31.00
MFoE	35.40	<u>34.21</u>	<u>30.26</u>	<u>31.20</u>
Prox-DRUNet	<u>35.32</u>	34.53	30.97	31.66

tuned on a validation set of 10 images, and the performance is reported on a testing set of 50 images, all normalized to the range $[0, 1]$.

The performance is reported in Table IV. Again, the MFoE outperforms the WCRR in every instance. It also manages to outperform Prox-DRUNet on the simpler instance with the PD data. Examples of reconstruction are provided in Figure 7.

3) *Computed Tomography*: We evaluate our method on the LoDoPaB-CT dataset [33], which contains ground-truth images derived from 2D slices of reconstructions in the LIDC/IDRI database [34], each of size (362×362) . The measurement operators are defined by parallel-beam geometry and implemented using the ASTRA Toolbox [35], [36]. All experiments are conducted with 256 simulated detectors. The resulting sinograms are corrupted with Gaussian noise of standard deviation $\sigma_w = 0.1$.

We consider three acquisition settings with 60, 40, and 20 projection angles, respectively. Each method is initialized

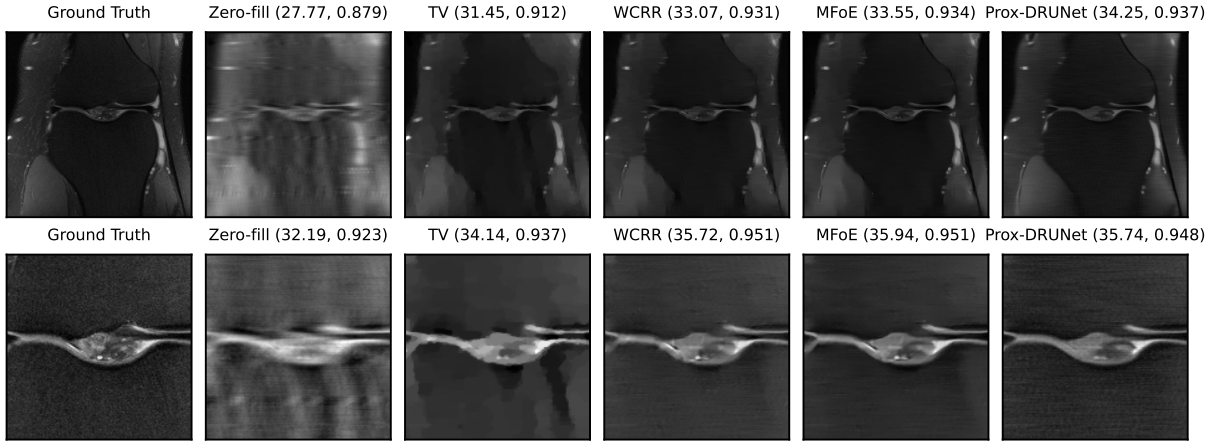


Fig. 7. Reconstruction for 8-fold subsampling and PDFS data. The reported metrics are (PSNR, SSIM).

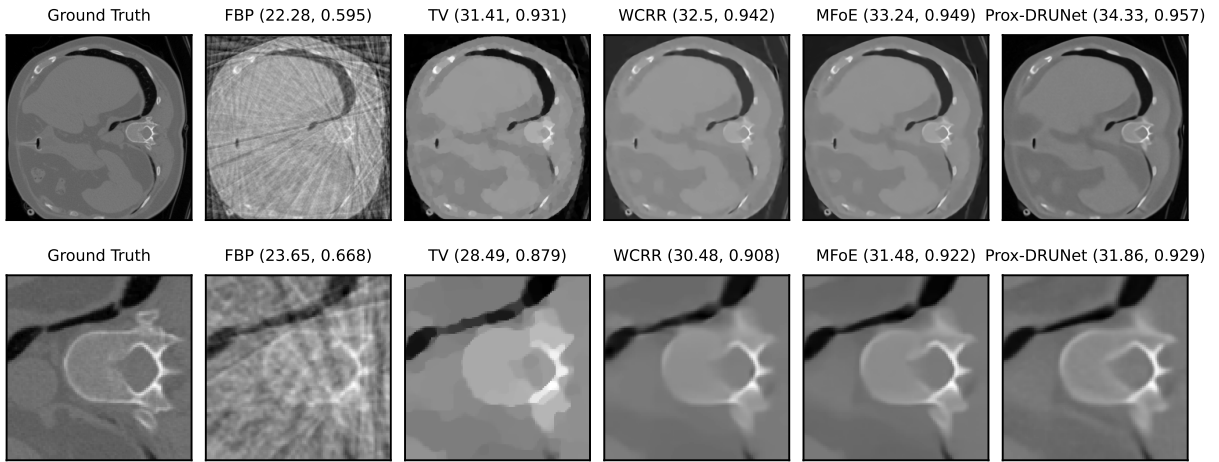


Fig. 8. Reconstruction for CT with 20 angles and 256 line detectors. The reported metrics are (PSNR, SSIM).

TABLE V
PSNR VALUES FOR CT RECONSTRUCTION ON THE LoDoBAP DATASET.

	60 angles	40 angles	20 angles
FBP	28.53	25.87	21.41
TV	33.74	32.58	30.11
WCRR	35.21	33.87	31.08
MFoE	35.45	34.22	31.54
Prox-DRUNet	35.73	34.61	32.12

TABLE VI
AVERAGE TIME PER IMAGE FOR ALL THE RECONSTRUCTION MODALITIES.

	Deblurring	CS-MRI	CT
TV	5.86	7.16	24.26
WCRR	6.45	6.89	13.90
MFoE	5.39	16.48	16.60
Prox-DRUNet	39.82	62.52	267.42

with the filtered-back projected (FBP) image, and the hyper-parameters are tuned on a validation set of 10 images. The performance is reported on a testing set of 50 images, all normalized to the range $[0, 1]$.

The performance is presented in Table V. There too, MFoE outperforms WCRR in all tested configurations. Examples of reconstruction are provided in Figure 8.

4) *Time Comparisons:* Table VI contains the average inference time per image, measured in seconds, for each inverse problem. More detailed results are provided in Tables VIII–X. These results highlight that the performance gains of Prox-DRUNet come at a computational cost. In particular, the CT reconstructions with Prox-DRUNet are significantly

slower than with other methods, as they require the repeated evaluation of the proximal operator of the data-fitting term—a step that is especially costly in the case of CT. By contrast, MFoE is only moderately more demanding than the WCRR in inference time, between 35% and 40% on average across all experiments due to the computational cost of the projection onto \mathcal{B}_{ℓ_1} .

Deep-learning-based methods such as Prox-DRUNet sets a high standard in learned regularization by leveraging a large number of parameters and extensive training data which contribute to their good performance across diverse tasks. We believe that MFoE offers an interesting alternative with significantly fewer parameters, fewer training data, faster inference time, and with a reconstruction quality that is close to

Prox-DRUNet. Together, these methods offer complementary strengths, providing valuable options suited to varying application needs.

V. CONCLUSION

We have proposed the MFoE model. It is a principled extension of the classic FoE model and incorporates multivariate potential functions via Moreau envelopes of the ℓ_∞ -norm. Our method offers improved adaptability across multiple inverse problems. The image quality that it achieves is comparable to that of state-of-the-art learned regularizers. It offers a clear structured design that is easy to implement with competitive reconstruction times.

ACKNOWLEDGEMENTS

The research leading to these results was supported by the European Research Council (ERC) under European Union’s Horizon 2020 (H2020), Grant Agreement - Project No 101020573 FunLearn.

REFERENCES

- [1] S. Roth and M. Black, “Fields of Experts: A framework for learning image priors,” in *2005 IEEE Computer Society Conference on Computer Vision and Pattern Recognition*, vol. 2, 2005, pp. 860–867.
- [2] Y. Chen, R. Ranftl, and T. Pock, “Insights into analysis operator learning: From patch-based sparse models to higher order MRFs,” *IEEE Transactions on Image Processing*, vol. 23, no. 3, pp. 1060–1072, 2014.
- [3] H. Q. Nguyen, E. Bostan, and M. Unser, “Learning convex regularizers for optimal Bayesian denoising,” *IEEE Transactions on Signal Processing*, vol. 66, no. 4, pp. 1093–1105, 2018.
- [4] A. Goujon, S. Neumayer, P. Bohra, S. Ducotterd, and M. Unser, “A neural-network-based convex regularizer for inverse problems,” *IEEE Transactions on Computational Imaging*, vol. 9, pp. 781–795, 2023.
- [5] A. Goujon, S. Neumayer, and M. Unser, “Learning weakly convex regularizers for convergent image-reconstruction algorithms,” *SIAM Journal on Imaging Sciences*, vol. 17, no. 1, pp. 91–115, 2024.
- [6] M. Zach, E. Kobler, A. Chambolle, and T. Pock, “Product of Gaussian mixture diffusion models,” *Journal of Mathematical Imaging and Vision*, vol. 66, no. 4, pp. 504–528, 2024.
- [7] M. Pourya, S. Neumayer, and M. Unser, “Iteratively refined image reconstruction with learned attentive regularizers,” *Numerical Functional Analysis and Optimization*, vol. 45, no. 7-9, pp. 411–440, 2024.
- [8] L. I. Rudin, S. Osher, and E. Fatemi, “Nonlinear total variation based noise removal algorithms,” *Physica D: Nonlinear Phenomena*, vol. 60, no. 1, pp. 259–268, 1992.
- [9] A. Chambolle, “An algorithm for total variation minimization and applications,” *Journal of Mathematical Imaging and Vision*, vol. 20, pp. 89–97, 2004.
- [10] H. V. Stackelberg, *Marktform und Gleichgewicht*. Springer, 1934.
- [11] S. V. Venkatakrisnan, C. A. Bouman, and B. Wohlberg, “Plug-and-play priors for model based reconstruction,” in *2013 IEEE Global Conference on Signal and Information Processing*, 2013, pp. 945–948.
- [12] E. Ryu, J. Liu, S. Wang, X. Chen, Z. Wang, and W. Yin, “Plug-and-Play methods provably converge with properly trained denoisers,” in *Proceedings of the 36th International Conference on Machine Learning*, ser. Proceedings of Machine Learning Research, vol. 97. PMLR, 2019, pp. 5546–5557.
- [13] S. Ducotterd, A. Goujon, P. Bohra, D. Perdios, S. Neumayer, and M. Unser, “Improving Lipschitz-constrained neural networks by learning activation functions,” *Journal of Machine Learning Research*, vol. 25, no. 65, pp. 1–30, 2024.
- [14] S. H. Chan, X. Wang, and O. A. Elgendy, “Plug-and-play ADMM for image restoration: Fixed-point convergence and applications,” *IEEE Transactions on Computational Imaging*, vol. 3, no. 1, pp. 84–98, 2017.
- [15] S. Hurault, A. Leclaire, and N. Papadakis, “Gradient step denoiser for convergent plug-and-play,” in *International Conference on Learning Representations*, 2022.
- [16] —, “Proximal denoiser for convergent plug-and-play optimization with nonconvex regularization,” in *Proceedings of the 39th International Conference on Machine Learning*. PMLR, 2022, pp. 9483–9505.
- [17] Z. Fang, S. Buchanan, and J. Sulam, “What’s in a prior? learned proximal networks for inverse problems,” in *International Conference on Learning Representations*, 2024.
- [18] J.-J. Moreau, “Proximité et dualité dans un espace hilbertien,” *Bulletin de la Société Mathématique de France*, vol. 93, pp. 273–299, 1965.
- [19] L. Condat, “Fast projection onto the simplex and the ℓ_1 ball,” *Mathematical Programming*, vol. 158, no. 1, pp. 575–585, 2016.
- [20] I. Selesnick, “Sparse regularization via convex analysis,” *IEEE Transactions on Signal Processing*, vol. 65, no. 17, pp. 4481–4494, 2017.
- [21] M. Unser and S. Ducotterd, “Universal architectures for the learning of polyhedral norms and convex regularizers,” *arXiv:2503.19190*, 2025.
- [22] E. Kobler, A. Effland, K. Kunisch, and T. Pock, “Total deep variation for linear inverse problems,” in *2020 IEEE/CVF Conference on Computer Vision and Pattern Recognition (CVPR)*, 2020, pp. 7546–7555.
- [23] B. O’Donoghue and E. Candès, “Adaptive restart for accelerated gradient schemes,” *Foundations of Computational Mathematics*, vol. 15, no. 3, pp. 715–732, 2015.
- [24] Z. Geng and J. Z. Kolter, “Torchdeq: A library for deep equilibrium models,” <https://github.com/locuslab/torchdeq>, 2023.
- [25] C. G. Broyden, “A class of methods for solving nonlinear simultaneous equations,” *Mathematics of Computation*, vol. 19, no. 92, pp. 577–593, 1965.
- [26] P. Arbeláez, M. Maire, C. Fowlkes, and J. Malik, “Contour detection and hierarchical image segmentation,” *IEEE Transactions on Pattern Analysis and Machine Intelligence*, vol. 33, no. 5, pp. 898–916, 2011.
- [27] K. Zhang, Y. Li, W. Zuo, L. Zhang, L. Van Gool, and R. Timofte, “Plug-and-play image restoration with deep denoiser prior,” *IEEE Transactions on Pattern Analysis and Machine Intelligence*, vol. 44, no. 10, pp. 6360–6376, 2022.
- [28] R. M. Gray, “Toeplitz and circulant matrices: A review,” *Foundations and Trends® in Communications and Information Theory*, vol. 2, no. 3, pp. 155–239, 2006.
- [29] K. Plataniotis, D. Androustos, and A. Venetsanopoulos, “Multichannel filters for image processing,” *Signal Processing: Image Communication*, vol. 9, no. 2, pp. 143–158, 1997.
- [30] M. Varma and A. Zisserman, “A statistical approach to texture classification from single images,” *International Journal of Computer Vision*, vol. 62, no. 1-2, pp. 61–81, 2005.
- [31] A. Levin, Y. Weiss, F. Durand, and W. T. Freeman, “Understanding and evaluating blind deconvolution algorithms,” in *2009 IEEE Conference on Computer Vision and Pattern Recognition*, 2009, pp. 1964–1971.
- [32] J. Zbonxtar, F. Knoll, A. Sriram, T. Murrell, Z. Huang, M. J. Muckley, A. Defazio, R. Stern, P. Johnson, M. Bruno, M. Parente, K. J. Geras, J. Katsnelson, H. Chandarana, Z. Zhang, M. Drozdal, A. Romero, M. Rabbat, P. Vincent, N. Yakubova, J. Pinkerton, D. Wang, E. Owens, C. L. Zitnick, M. P. Recht, D. K. Sodickson, and Y. W. Lui, “fastMRI: An open dataset and benchmarks for accelerated MRI,” *arXiv:1811.08839*, 2018.
- [33] J. Leuschner, M. Schmidt, D. O. Bagger, and P. Maass, “LoDoPaB-CT, a benchmark dataset for low-dose computed tomography reconstruction,” *Scientific Data*, vol. 8, no. 1, p. 109, 2021.
- [34] S. G. Armato III, G. McLennan, L. Bidaut, M. F. McNitt-Gray, C. R. Meyer, A. P. Reeves, B. Zhao, D. R. Aberle, C. I. Henschke, E. A. Hoffman *et al.*, “The lung image database consortium (LIDC) and image database resource initiative (IDRI): A completed reference database of lung nodules on CT scans,” *Medical physics*, vol. 38, no. 2, pp. 915–931, 2011.
- [35] W. van Aarle, W. J. Palenstijn, J. Cant, E. Janssens, F. Bleichrodt, A. Dabrovolski, J. D. Beenhouwer, K. J. Batenburg, and J. Sijbers, “Fast and flexible x-ray tomography using the astra toolbox,” *Optics Express*, vol. 24, pp. 25 129–25 147, 2016.
- [36] W. J. Palenstijn, K. J. Batenburg, and J. Sijbers, “Performance improvements for iterative electron tomography reconstruction using graphics processing units (GPUs),” *Journal of Structural Biology*, vol. 176, pp. 250–253, 2011.
- [37] R. T. Rockafellar, “Monotone operators and the proximal point algorithm,” *SIAM Journal on Control and Optimization*, vol. 14, no. 5, pp. 877–898, 1976.
- [38] H. H. Bauschke and P. L. Combettes, *Convex Analysis and Monotone Operator Theory in Hilbert Spaces*, ser. CMS Books in Mathematics, 2011.

APPENDIX

A. Proof of Theorem 1

We omit subscripts for clarity. By definition, we have that

$$\begin{aligned}
\rho_{\tau\mu}^d(\mathbf{Q}\mathbf{x}) &= \inf_{\mathbf{z} \in \mathbb{R}^d} \left(\|\mathbf{z}\|_\infty + \frac{1}{2\tau\mu} \|\mathbf{z} - \mathbf{Q}\mathbf{x}\|_2^2 \right) \\
&\leq \|\mathbf{Q} \text{prox}_{\mu\|\cdot\|_\infty}(\mathbf{x})\|_\infty + \frac{1}{2\tau\mu} \|\mathbf{Q} \text{prox}_{\mu\|\cdot\|_\infty}(\mathbf{x}) - \mathbf{Q}\mathbf{x}\|_2^2 \\
&\leq \|\text{prox}_{\mu\|\cdot\|_\infty}(\mathbf{x})\|_\infty + \frac{1}{2\mu} \frac{\|\mathbf{Q}\|_2^2}{\tau} \|\text{prox}_{\mu\|\cdot\|_\infty}(\mathbf{x}) - \mathbf{x}\|_2^2 \\
&= \|\mathbf{x} - \mu \text{Proj}_{\mathcal{B}_{\ell_1}}(\mathbf{x}/\mu)\|_\infty + \frac{\mu}{2} \frac{\|\mathbf{Q}\|_2^2}{\tau} \|\text{Proj}_{\mathcal{B}_{\ell_1}}(\mathbf{x}/\mu)\|_2^2.
\end{aligned} \tag{20}$$

It follows that

$$\rho_\mu^d(\mathbf{x}) - \rho_{\tau\mu}^d(\mathbf{Q}\mathbf{x}) \geq \frac{\mu}{2} \left(1 - \frac{\|\mathbf{Q}\|_2^2}{\tau} \right) \|\text{Proj}_{\mathcal{B}_{\ell_1}}(\mathbf{x}/\mu)\|_2^2. \tag{21}$$

This lower bound is positive for all $\mathbf{x} \neq \mathbf{0}$. In contrast, when $\mathbf{x} = \mathbf{0}$, the two Moreau envelopes vanish and the function attains its minimum. Therefore, $\psi(\mathbf{x})$ is nonnegative with a unique zero-valued global minimum at the origin.

We now consider the gradient of $\psi(\mathbf{x})$ given by

$$\nabla\psi(\mathbf{x}) = \mu \text{Proj}_{\mathcal{B}_{\ell_1}}(\mathbf{x}/\mu) - \mu \mathbf{Q}^T \text{Proj}_{\mathcal{B}_{\ell_1}}(\mathbf{Q}\mathbf{x}/\tau\mu). \tag{22}$$

Let $P = \mu \text{Proj}_{\mathcal{B}_{\ell_1}}(\cdot/\mu)$, the proximal operator of the indicator function of the set $\{\mathbf{z} \in \mathbb{R}^d : \|\mathbf{z}\|_1 \leq \mu\}$. It is therefore a firmly nonexpansive mapping [37], so that

$$\|P(\mathbf{x}) - P(\mathbf{y})\|_2^2 \leq \langle P(\mathbf{x}) - P(\mathbf{y}), \mathbf{x} - \mathbf{y} \rangle \quad \forall \mathbf{x}, \mathbf{y} \in \mathbb{R}^d. \tag{23}$$

We show that $\mathbf{Q}^T \text{Proj}_{\mathcal{B}_{\ell_1}}(\mathbf{Q} \cdot / \tau\mu) = \mathbf{Q}^T P(\mathbf{Q} \cdot / \tau)$ is also firmly nonexpansive. This comes from the relations

$$\begin{aligned}
&\left\| \mathbf{Q}^T P\left(\frac{\mathbf{Q}\mathbf{x}}{\tau}\right) - \mathbf{Q}^T P\left(\frac{\mathbf{Q}\mathbf{y}}{\tau}\right) \right\|_2^2 \\
&\leq \|\mathbf{Q}\|_2^2 \left\| P\left(\frac{\mathbf{Q}\mathbf{x}}{\tau}\right) - P\left(\frac{\mathbf{Q}\mathbf{y}}{\tau}\right) \right\|_2^2 \\
&\leq \|\mathbf{Q}\|_2^2 \left\langle P\left(\frac{\mathbf{Q}\mathbf{x}}{\tau}\right) - P\left(\frac{\mathbf{Q}\mathbf{y}}{\tau}\right), \frac{\mathbf{Q}\mathbf{x}}{\tau} - \frac{\mathbf{Q}\mathbf{y}}{\tau} \right\rangle \\
&= \frac{\|\mathbf{Q}\|_2^2}{\tau} \left\langle \mathbf{Q}^T P\left(\frac{\mathbf{Q}\mathbf{x}}{\tau}\right) - \mathbf{Q}^T P\left(\frac{\mathbf{Q}\mathbf{y}}{\tau}\right), \mathbf{x} - \mathbf{y} \right\rangle \\
&\leq \left\langle \mathbf{Q}^T P\left(\frac{\mathbf{Q}\mathbf{x}}{\tau}\right) - \mathbf{Q}^T P\left(\frac{\mathbf{Q}\mathbf{y}}{\tau}\right), \mathbf{x} - \mathbf{y} \right\rangle.
\end{aligned} \tag{24}$$

As shown in [38], every firmly nonexpansive operator is half averaged, meaning there exists nonexpansive mappings H_1, H_2 such that $P = \frac{1}{2} \text{Id} + \frac{1}{2} H_1$ and $\mathbf{Q}^T P(\mathbf{Q} \cdot / \tau\mu) = \frac{1}{2} \text{Id} + \frac{1}{2} H_2$. Applying this decomposition to $\nabla\psi$, we get that

$$\begin{aligned}
&\|\nabla\psi(\mathbf{x}) - \nabla\psi(\mathbf{y})\|_2 \\
&\leq \frac{1}{2} \|H_1(\mathbf{x}) - H_1(\mathbf{y})\|_2 + \frac{1}{2} \|H_2(\mathbf{x}) - H_2(\mathbf{y})\|_2 \\
&\leq \|\mathbf{x} - \mathbf{y}\|_2.
\end{aligned} \tag{25}$$

This proves that $\nabla\psi$ is nonexpansive.

TABLE VII
DENOISING PERFORMANCE ON THE BSD68 TEST SET.

	$\sigma = 15/255$	$\sigma = 25/255$	$\sigma = 50/255$
MFoE ($K = 60, d = 1$)	31.19	28.68	25.76
MFoE ($K = 30, d = 2$)	31.31	28.82	25.91
MFoE ($K = 20, d = 3$)	31.31	28.83	25.90
MFoE ($K = 15, d = 4$)	31.32	28.84	25.92
MFoE ($K = 12, d = 5$)	31.30	28.82	25.90
MFoE ($K = 10, d = 6$)	31.29	28.81	25.90
MFoE ($K = 6, d = 10$)	31.26	28.78	25.87
MFoE ($K = 5, d = 12$)	31.26	28.80	25.89
MFoE ($K = 4, d = 15$)	31.23	28.77	25.84
MFoE ($K = 3, d = 20$)	31.19	28.73	25.81
MFoE ($K = 2, d = 30$)	31.16	28.71	25.81
MFoE ($K = 1, d = 60$)	31.01	28.59	25.70

B. Implementation of WCRR-Free

To implement WCRR-free, we closely follow the approach of [5], parameterizing the potential function ψ via its derivative φ as

$$\varphi = \mu_+ \varphi_+ - \mu_- \varphi_-, \tag{26}$$

where $\mu_+, \mu_- > 0$ are learnable scalar weights and φ_+, φ_- are trainable, nondecreasing, nonexpansive linear splines. The only deviation from [5] is that we allow μ_- to be learnable, whereas it was fixed to $\mu_- = 1$ in the original implementation. We assign to μ_- the same learning rate as μ_+ .

C. Implementation of MFoE- ℓ_2

Let $\eta_\mu^d: \mathbb{R}^d \rightarrow \mathbb{R}_+$ denote the Moreau envelope of the ℓ_2 -norm. Using (7)–(9), it can be expressed as

$$\eta_\mu^d(\mathbf{x}) = \|\mathbf{x} - \mu \text{Proj}_{\mathcal{B}_{\ell_2}}(\mathbf{x}/\mu)\|_2 + \frac{\mu}{2} \|\text{Proj}_{\mathcal{B}_{\ell_2}}(\mathbf{x}/\mu)\|_2^2, \tag{27}$$

where

$$\mathcal{B}_{\ell_2} = \{\mathbf{z} \in \mathbb{R}^d : \|\mathbf{z}\|_2 \leq 1\} \tag{28}$$

denotes the unit ℓ_2 -ball in \mathbb{R}^d . We build the potentials as

$$\psi(\mathbf{x}) = \mu \eta_\mu^d(\mathbf{x}) - \mu \eta_{\tau\mu}^d(\mathbf{Q}\mathbf{x}). \tag{29}$$

To ensure the same guarantees as in Theorem 1, it is sufficient to impose that $\|\mathbf{Q}\|_2 \leq 1$ and $\tau > 1$. With the exact same mathematical manipulations as (20), we can show that

$$\eta_\mu^d(\mathbf{x}) - \eta_{\tau\mu}^d(\mathbf{Q}\mathbf{x}) \geq \frac{\mu}{2} \left(1 - \frac{\|\mathbf{Q}\|_2^2}{\tau} \right) \|\text{Proj}_{\mathcal{B}_{\ell_2}}(\mathbf{x}/\mu)\|_2^2. \tag{30}$$

This allows us to draw the same conclusions as in Section A. The gradient of $\psi(\mathbf{x})$ given by

$$\nabla\psi(\mathbf{x}) = \mu \text{Proj}_{\mathcal{B}_{\ell_2}}(\mathbf{x}/\mu) - \mu \mathbf{Q}^T \text{Proj}_{\mathcal{B}_{\ell_2}}(\mathbf{Q}\mathbf{x}/\tau\mu) \tag{31}$$

can also be proven to be nonexpansive with the exact same arguments as in Section A.

D. Additional Denoising Results

We provide the results in Table VII.

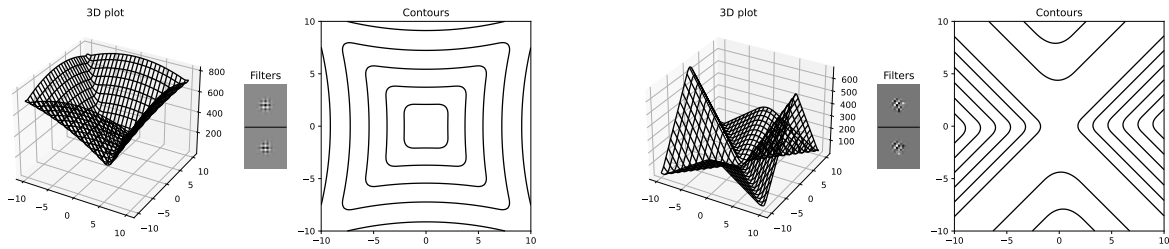


Fig. 9. Learned potential functions and corresponding filters for two selected groups.

TABLE VIII
AVERAGE RECONSTRUCTION TIME PER IMAGE IN DEBLURRING.

						
	$\sigma_w = 0.01$	$\sigma_w = 0.03$	$\sigma_w = 0.01$	$\sigma_w = 0.03$	$\sigma_w = 0.01$	$\sigma_w = 0.03$
TV	9.70 ± 2.44	5.39 ± 1.26	5.93 ± 1.26	3.47 ± 0.70	6.32 ± 1.18	4.33 ± 0.77
WCRR	4.75 ± 1.70	4.95 ± 1.41	7.03 ± 1.60	7.35 ± 1.86	7.54 ± 1.47	7.07 ± 1.88
MFoE	5.56 ± 1.35	4.17 ± 0.93	6.38 ± 1.34	5.14 ± 0.97	6.17 ± 1.21	4.93 ± 0.86
Prox-DRUNet	21.87 ± 11.47	20.33 ± 11.76	37.42 ± 16.86	45.17 ± 15.19	39.16 ± 15.57	74.95 ± 22.51

TABLE IX
AVERAGE RECONSTRUCTION TIME PER IMAGE IN CS-MRI.

	$(M_{\text{acc}} = 4, M_{\text{cf}} = 0.08)$		$(M_{\text{acc}} = 8, M_{\text{cf}} = 0.04)$	
	PD	PDFS	PD	PDFS
TV	4.89 ± 0.98	6.83 ± 1.28	9.93 ± 1.60	7.00 ± 1.60
WCRR	5.72 ± 1.71	4.46 ± 1.34	10.91 ± 1.90	6.48 ± 1.83
MFoE	14.64 ± 3.32	7.78 ± 1.52	26.04 ± 4.66	17.47 ± 4.25
Prox-DRUNet	73.32 ± 20.55	41.06 ± 15.69	67.78 ± 16.08	67.90 ± 14.06

TABLE X
AVERAGE RECONSTRUCTION TIME PER IMAGE IN CT.

	60 angles	40 angles	20 angles
TV	24.12 ± 2.59	25.02 ± 2.93	23.63 ± 1.45
WCRR	13.96 ± 1.82	14.16 ± 1.31	13.58 ± 2.18
MFoE	13.75 ± 3.69	15.92 ± 4.19	20.13 ± 3.63
Prox-DRUNet	266.98 ± 209.95	308.04 ± 124.73	368.30 ± 126.36

E. Plot of Potentials

We show additional potentials in Figure 9.

F. Time Comparisons

We provide the results in Tables VIII, IX, and X.